Mechanism of hot crack propagation and prevention of crack formation during electron beam powder bed fusion of a difficult-to-weld Co-Cr-Ni-W superalloy

M.A.L. Phan[1*], D. Fraser[2], S. Gulizia[2] and Z.W. Chen[3]

1. Department of Materials Science and Engineering, The University of Sheffield, UK
2. CSIRO Manufacturing, Victoria, Australia
3. Department of Mechanical Engineering, Auckland University of Technology, NZ

* Corresponding author: m.phan@sheffield.ac.uk

Abstract

Understanding how hot cracks propagate in difficult-to-weld alloys during electron beam powder bed fusion (EBPBF) is necessary for manufacturing quality parts. The current understanding in the literature does not go into sufficient details of the mechanisms of crack propagation. The major part of this study aimed to reveal how cracks grow during EBPBF. Samples were made using EBPBF of a Co-base alloy that is a difficult-to-weld type and crack patterns/networks were revealed through sequential sectioning-polishing, which is a new way of illustrating hot crack networks. It was found that when surface cracks were observed, they tended to orientate normal to the scan direction. The scan direction changed 90° after each layer and the surface cracks also changed orientations accordingly. The relationships between the crack orientations on the surface and the crack networks beneath the top layer were observed. The identification of how the crack networks had grown and how liquation had assisted this growth is shown. Sometimes surface cracking was found to be absent even though the crack network beneath the top layer kept developing. The lack of surface cracking is explained by the natural growth of a horizontal dendritic surface layer that is formed under the condition of a low tangent angle melt track. Thus, the second part of the study was an attempt to utilize horizontal dendrites for hot crack prevention. It will be shown that controlled remelting can be an effective method to preserve the horizontal dendrite grains in each scan layer and thus hot cracking does not occur. It will be further shown also that controlled remelting can occasionally result in equiaxed grain growth.

Keywords: Columnar grain growth; liquation and hot tear; crack network; horizontal dendrites

1. Introduction

Electron beam powder bed fusion (EBPBF) is one of the two PBF metal additive manufacturing (MAM) processes. The other is laser powder bed fusion (LPBF). During PBF, the energy beam fully and rapidly fuses the powder in a selective path instructed by a programme that forms from slicing parts created in 3D CAD models. Thus, PBF allows geometrically complex parts to be manufactured. Ti alloys which are readily weldable are being commonly processed by both EBPBF and LPBF. For wider industrial applications of PBF processes, a deeper understanding of the processability of the traditionally difficult-to-weld or non-weldable alloys is of interest in the literature. Babu et al. (2018) have explained that the strong research effort in the field of PBF of Ni-based superalloys is because of the large potential interest to the aerospace industry. They also described the major challenge of achieving high quality PBF parts relates to grain growth and

thermal stresses during PBF and that they may result in hot cracking within the parts. Process control to reduce hot cracking is also considered an important aspect of the research.

Eskin and Katgerman (2004) explained that hot cracking, originally known as hot tearing in casting, normally occurs at the final stage of solidification. In fusion welding, hot cracking can be in two different forms. The first is hot tearing also in the final stage of solidification in fusion zone and the second is liquation cracking in the partially melted zone. In comparison to LPBF, an advantage of EBPBF is that its bed temperature is normally higher than 500°C and thus thermal gradients and stresses should be lower. Despite this, hot cracking of difficult-to-weld alloys such as some Ni-superalloys also occurs extensively. A study by Chauvet et al. (2018a) has aimed to understand the mechanism of hot cracking during EBPBF using a non-weldable Ni-based alloy. In their work, cracks propagated along the grain boundaries (GB) of the long columnar grains over many layers. They undertook tensile testing with the loading direction of the samples normal to the build direction (BD). They found the presence of a fully dendritic morphology observed on the tensile sample fracture surfaces was the basis to favour solidification cracking (hot tearing) as being the cracking mechanism. However, they recognise the difficulty of discriminating liquation cracking and solidification cracking.

Peng et al. (2018) also commented that a positive identification of liquation cracking could not be made in their work. They found that cracking solely propagated along the columnar grain boundaries and they were unable to identify track boundaries. Because of this, they referred to the cracking as liquid-state cracking, following Chauvet et al. (2018a). Kontis et al. (2019) have conducted an analysis on the composition of columnar grain boundaries using atom probe. They illustrated how solutes segregated along grain boundaries, but particularly on high angle grain boundaries where the cracks formed. They suggested this was a strong indication of grain boundary liquation as being the cause of hot cracking. Finally, they observed a crack reaching the bottom boundary of the last solidified melt layer. They suggested this was an indication that there was no continuation of the crack during solidification of the layer. This is however not consistent with the earlier micrograph evidence by Chauvet et al. (2018a) who found that hot cracks readily reach the surface during EBPBF of a Ni-based superalloy. More recently, Chandra et al. (2021) have considered a general hot cracking criterion for EBPBF, but this has been purely based on hot tearing during solidification and liquation has not been considered.

During PBF, the scan direction (SD) commonly changes by a specific angle every layer (e.g. 90^{o} in EBPBF). Changing in SD should alter direction of thermal stresses accordingly, which may affect the way hot cracks propagate. Cloots et al. (2016) reported that hot cracks during LPBF of IN738LC always orientate transversely to SD in the last layer for either 0^{o} or 90^{o} rotation of SD after each layer. Ramirez et al. (2011) observed cracks that appear on the surface are more dominant in the direction normal to SD. In contrast, Lee et al. (2020) reported that hot cracks occasionally appear in layers having SD likely aligns with the cracks' orientation. In previous studies on crack formation in EBPBF, such as those by Chauvet et al. (2018a), Kontis et al. (2019), and Peng et al. (2018), it has not been fully demonstrated how crack orientation relates to the direction of stresses and how crack networks develop within a layer and inter-layers. Therefore,

the hot cracking phenomena during PBF is considered to be insufficiently understood. This is also reviewed as an essential research area by DebRoy et al. (2019). Despite this, a solution for crack-free samples in EBPBF has been shown to be achievable. Chauvet et al. (2018b) produced a single-crystal crack free cylinder sample in EBPBF of a Ni-based alloy, although in complex parts their method of producing single-crystal is not practically achievable. In contrast, Kontis et al. (2019) control the EBPBF process to obtain equiaxed grains instead of columnar grains of a Ni-based alloy. The authors successfully achieved crack free samples; however, the processing details are not clearly explained. Obtaining equiaxed grains using normal EBPBF manufacturing condition remains a large challenge. Thus, it is necessary to study an alternative method to eliminate hot cracking within the normal EBPBF process windows.

In the present work, EBPBF experiments have been conducted using a Co-Cr-Ni-W superalloy, which is a difficult-to-weld alloy. In order to understand how cracks have grown layer by layer with normal EBPBF conditions, the 3D crack networks in samples were examined parallel and perpendicular to the build direction. The growth and continuity of cracks can then be related to the scanning direction. Also, it allows the liquation and hot tearing along grain boundaries to be identified. In addition, a numerical simulation has been conducted in order to understand how temperature distributions within the scanned tracks relate to hot cracking. The numerical simulation was also conducted to allow a visualisation of the shape of the melt pool after one or more track scans.

In a previous study using the same difficult-to-weld Co-Cr-Ni-W superalloy, Phan et al. (2018) reported that a top layer of columnar dendrites can grow horizontally within each scan layer in low tangent angle tracks. A low tangent angle refers to a low angle between the build direction and the tangent at the end of the track boundary (reaching the track surface) in the cross section normal to scan direction. Horizontally grown dendrites should result in a crack not propagating through this region since hot cracks largely grow along build direction and will be stopped by this boundary. Thus, in this present study, an attempt has also been made to control EBPBF process parameters so that the layer of dendrites grown horizontally is not completely melted. Thus, a grain architecture comprising of horizontal and vertical (H-V) columnar grains alternatively layer after layer can be produced and be demonstrated. This grain structure effectively stops the growth or prevents the initiation of cracks that are dominantly in build direction during EBPBF.

2. Materials and Methods

2.1. Experimental procedure

Cubic samples with a size of 20mm×20mm×10mm were made using an Arcam® A1 SEBM machines. The default value of accelerated voltage was 60 kV and the build chamber was vacuumed to10^{-4}-10^{-5} mbar. The powder material used was produced using gas atomization process and the composition of the initial powder was Co-27Cr-11Ni-7W. The powder particle size was measured using Malver Mastersizer S and the size distribution is D10 = 55.7 µm, D50 = 76.2 µm and D90 = 105.7 µm. For EBPBF, the start plate was preheated to 900 °C. The build stage was lowered by 70 µm after each layer. SD alternated by rotating 90^{o} after every layer, which is

the common scanning strategy for SEBM. Two processing conditions were used, and they differ in the value of focus offset while the line offset (spacing) at 0.1 mm and the speed function at 25 were kept unchanged. In EBPBF, a speed function value refers to a certain combination of beam current and scan speed. A value of speed function at 25 is a common value used for running EBPBF. In condition 1 the focus offset value was 25 mA and thus the sample is named F25. In condition 2 focus offset value was 50 mA, named F50. The beam spot size ranges 400 μm to 1,000 μm, as specified by EBPBF machine manufacturer. A lower focus offset value means a lower beam spot size.

Fig. 1 schematically shows the sectioning for metallography in an EBPBF sample with the cross sections in reference to Building Direction (BD) and Scanning Direction (SD) in the final layer. As will be presented, cracks which are largely parallel to BD can be readily observed in x-z and y-z cross sections. Cracks were also revealed on a series of x-y sections by consecutively grinding-polishing from the top layer down along the Z direction. For this, micro-indentation was employed using an indenter with a fixed pyramidal shape having a known face angle of 136°. The applied force was selected at 1 kg and the dwell time was 10 s. These resulted in an impression depth of 15 ~ 16 μm. The micro-indentation was done at several locations throughout the examined surface to mark an even depth and ensured an even grinding layer by layer. After mechanical polishing, samples were electrolytically polished/etched with 10% H_2SO_4 + 90% CH_3OH solution at 6 V for 10 s. Samples were examined using a Hitachi 70-SU field emission scanning electron microscope (SEM) with electron back-scatter diffraction (EBSD) capability.

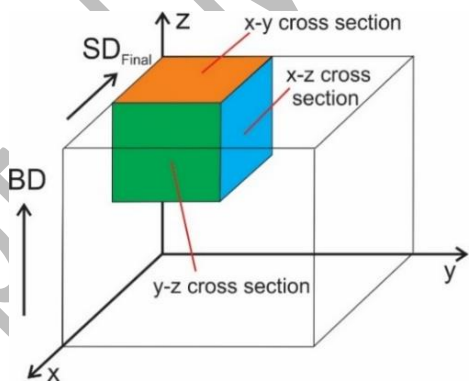

Fig. 1 Illustration of cross section sampling orientations

2.2. Simulation for temperature distribution

The ANSYS Mechanical APDL v.16.2 program was used to numerically simulate a 20-tracks scan (Fig. 2). The following non-linear heat transfer equation is used for transient thermal analysis in the ANSYS Mechanical APDL:

$$k\left(\frac{\partial^2 T}{\partial x^2}+\frac{\partial^2 T}{\partial y^2}+\frac{\partial^2 T}{\partial z^2}\right)+Q_{int}=\rho c_p\frac{\partial T}{\partial t} \qquad (1)$$

where Q_{int} is the internal heat source, T is temperature, k, c_p and ρ are thermal conductivity, specific heat and density of material, respectively. For the internal heat source Q_{int}, a Gaussian surface heat flux profile was employed and expressed by the following equations:

$$Q = Q_0 \exp(-\frac{2r^2}{r_0^2}) \quad (2)$$

$$Q_0 = \frac{2\eta VI}{\pi r_0^2} \quad (3)$$

where Q is absorbed heat flux, r is the radial distance from the centre of the heat source, r_o is the beam radius, η is the beam absorption efficiency coefficient, V is the voltage, and I is the beam current. Details of parameters used for Eq. 1 and Eq. 2 are shown in Table 1 and Fig. 2a. The 3D block model has dimensions of 5mm×20mm×3mm (x×y×z) and comprises of two different volumes, as illustrated in Fig. 2b. The first volume is the solid portion and the second one represents the deposited powder layer.

Table 1. Parameters used for the simulation study of temperature distribution.

Parameters	Values
Accelerated voltage V, V	60000
Beam current I, A	0.0057
Absorption efficiency η, %	90
Assumed beam radius r_o, m	0.0005
Scanning Speed, m/s	0.4
Start plate temperature, °C	900

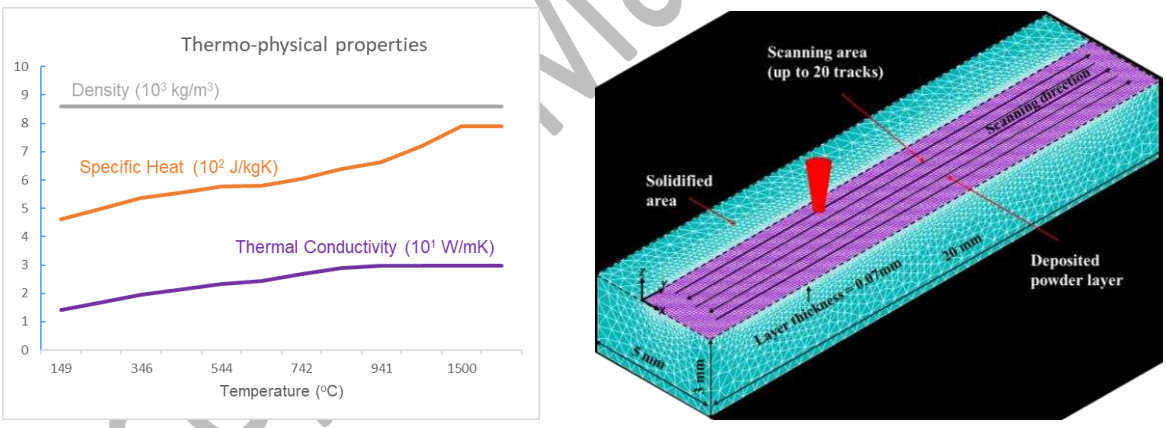

(a) (b)

Fig. 2 (a) Thermo-physical properties of Co-27Cr-11Ni-7W alloy and (b) Illustration showing the 3D meshed model used in simulation of a 20-tracks scanning.

In this simulation, the thermal conductivity was assumed to be isotropic, thus $k_{xx} = k_{yy} = k_{zz}$. A start plate preheating temperature of 900°C was used as an initial condition for the simulation. The boundary conditions are the convective and radiative heat flux losses from the top surface. However, in EBPBF, parts are fabricated in a vacuum build chamber, therefore, heat loss due to convection can be neglected. The remaining radiative heat loss is defined as:

$$q_{rad} = \varepsilon \times \rho\left(T^4 - T_o{}^4\right) \quad (4)$$

where T_o is the start plate preheating temperature, σ is the Stefan-Boltzmann constant and ε is the emissivity.

2.3. Parameters for H-V grain growth

The initial experiments, analysis and simulation as described above was aiming to identify and explain the mechanism of hot cracking. A further experimental test attempted to use a rotating horizontal and vertical (H-V) grain architecture to prevent hot cracking. The experimental steps of this latter attempt are now described. In order to produce horizontal and vertical (H-V) columnar grains alternatively layer after layer, the H-dendrites grown on top of each layer (Fig. 3a) should not be melted during next layer scan. For this, a focus offset 25 mA was used which result in a sufficiently low tangent angle between BD and the tangent of track boundary meeting the top surface and a H-dendrite top layer within the scan layer. The volumetric energy density (E_{Vol}) was employed as an indicator for tuning of EB-PBF process where multiple parameters are involved:

$$E_{Vol} = \frac{U.I}{v.t.h} \qquad (5)$$

where U is the accelerated voltage (=60 kV), I is the beam current, v is the scan speed, t is the layer thickness and h is the line offset. In EB-PBF, I and v and thus I/v are regulated by speed function set at 25 in this work.

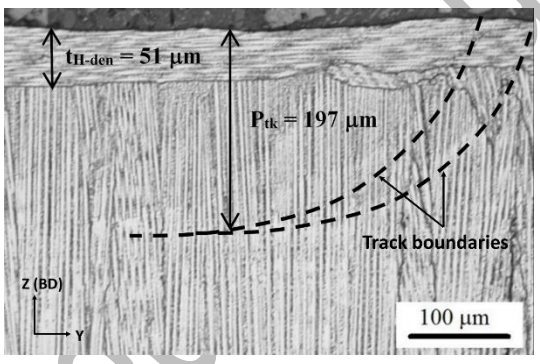

(a)

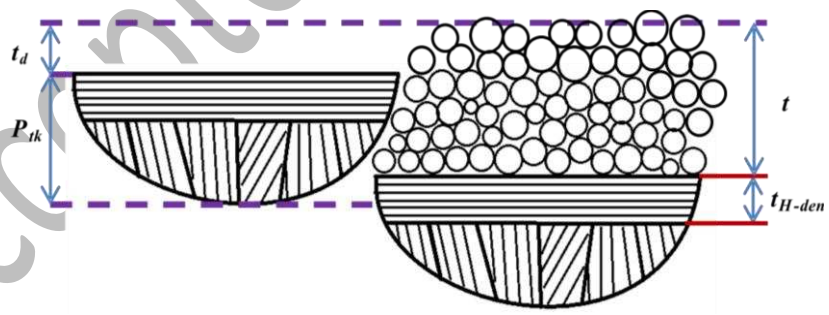

(b)

Fig. 3 (a) The low tangent angle track with H-dendrites obtained from sample built with line offset 0.1mm and layer thickness 70µm and (b) Illustration on the layer thickness adjustment to maintain H-dendrites.

H-dendrites form at the build surface for samples built with t = 70 µm and h = 0.1 mm. The track has a penetration depth (P_{tk}) of 197 µm and the thickness of H-dendrites thickness ($t_{H\text{-}den}$) being ~50 µm, as shown in Fig. 3a. Half (the non-melted) track boundary can be observed by slightly de-focusing using optical microscopy. To not completely melt the H-dendrite layer, the bottom of

the track deposited in the successive layer should be within $t_{H\text{-}den}$ of the present layer, as shown in Fig. 3b. The consolidated track will have its surface lower than the surface of the deposited powder layer with a distance of t_d. However, the value of this t_d is difficult to experimentally obtain but can be treated approximately as $t/2$, as an attempt. Then, in order not for the H-dendrite layer to completely melt, the following condition needs to be satisfied:

$$P_{tk} + t_d < t + t_{H\text{-}den} \qquad (6)$$

with $t_d \approx t/2$.

Then:

$$P_{tk}\ (197\mu m) + t_d < t + t_{H\text{-}den}\ (51\ \mu m)$$

$$t - t/2 > 146\ \mu m$$

$$t > 292\ \mu m \qquad (7)$$

Following (7), a layer thickness t_2 = 300 µm is selected together with h = 0.1mm. This leads to a significant reduction in E_{Vol} from:

$$E_{vol-1} = \frac{U \times I}{v \times t_1 \times h_1} = \frac{U \times I}{v \times 70\mu m \times 0.1mm}$$

to:

$$E_{vol-2} = \frac{U \times I}{v \times t_2 \times h_1} = \frac{U \times I}{v \times 300\mu m \times 0.1mm}$$

Changing E_{Vol} does not necessarily change the track shape. However, defects such as lack of fusion (LOF) may form. Thus, a further $E_{vol\text{-}3}$ is used by reducing h to 0.05 mm while t_2 is kept at 300 µm:

$$E_{vol-3} = \frac{U.I}{v \times t_2 \times h_3} = \frac{U.I}{v \times 300\mu m \times 0.05mm}$$

3. Results and Discussion

3.1 Cracks observed on sample surfaces and on cross sections

The surface appearance of samples built with the two different conditions are shown in Fig. 4. In the figure, the scan tracks of sample F25 are more readily identified than those in sample F50. The appearance of tear-drop ripples indicative of the tear-drop shaped melt during EBPBF was absent. Instead, wave-front ripples can be recognised, which was the result of track-long melts and has been explained by Phan et al. (2018). A distinctive surface difference for the two conditions, however, is the appearance of cracks. For sample F25, observing the surface as in Fig. 4a, a few cracks can be identified, and a small crack has been indicated in the figure. The crack is not only small but also appears straight and is orientated almost normal to SD. On the other hand, in sample F50, there are many cracks which appear irregular (rugged). Because they are not straight cracks, their orientations are not very meaningful, but they do appear orientated to some extent normal to

SD. In other words, it was relatively easy to find a portion of a crack largely normal to SD, but it was rare to find a local crack section parallel to SD.

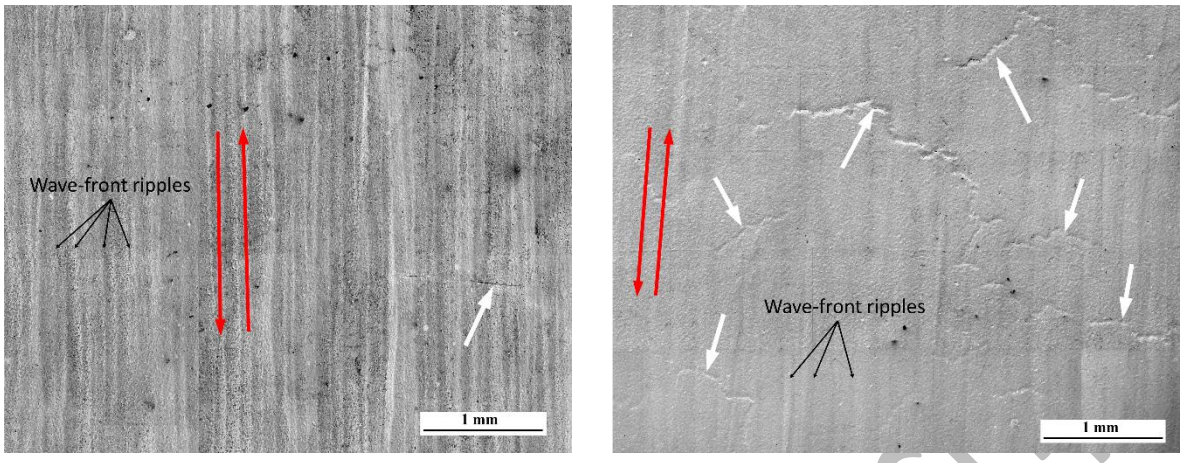

(a) (b)

Fig. 4 Top surface appearance of samples built with (a) F25 condition and (b) F50 condition. Scan directions (SD) are indicated by red and cracks are pointed to by white arrows. "Wave-front ripples" are also indicated.

Cross-sectional micrographs of samples built with the two EBPBF conditions are shown in Fig. 5. Long columnar grains, that are the common microstructural feature of EBPBF, are clearly seen in all micrographs. The top region of sample F25, which is up to 80 μm in thickness, is also columnar grains but they have grown in the direction normal to BD. These grains are horizontal dendrite (H-dendrites) grains and the reason for their growth direction, which was the result of a low tangent angle melt track with the more focus beam (than that of F50), has been explained previously by Phan et al. (2018). On the other hand, in sample F50, there is not H-dendrites top region. The reason for this has also been explained by Phan et al. (2018), being the result of a wider melt track (W_{Tk}) with a smaller track penetration (P_{Tk}) associated with having a larger beam size with F50 condition comparing to the beam size of F25 condition.

Cracks are the clear and common feature in Fig. 5 for the samples made in both conditions and the cracks were clearly the result of cracking along the intercolumnar grain boundaries. In sample F25, as shown in Fig. 5a, cracks did not reach the surface and stopped when they meet H-dendrites. The different surface appearances, comparing that of Fig. 4a to that of Fig. 4b, can now be understood. There was no intercolumnar grain boundaries for cracks to continue to the surface in the H-dendrite layer for condition F25. In other words, H-dendrites have covered the vertically grown cracks underneath (Fig. 5a). The small crack observed in Fig. 4a was the result of hot cracking within the H-dendrite layer. As has already been explained, the thickness of H-dendrites was up to 80 μm. The subsequent remelting of these dendrites means they have not affected the overall growth of cracks grown vertically.

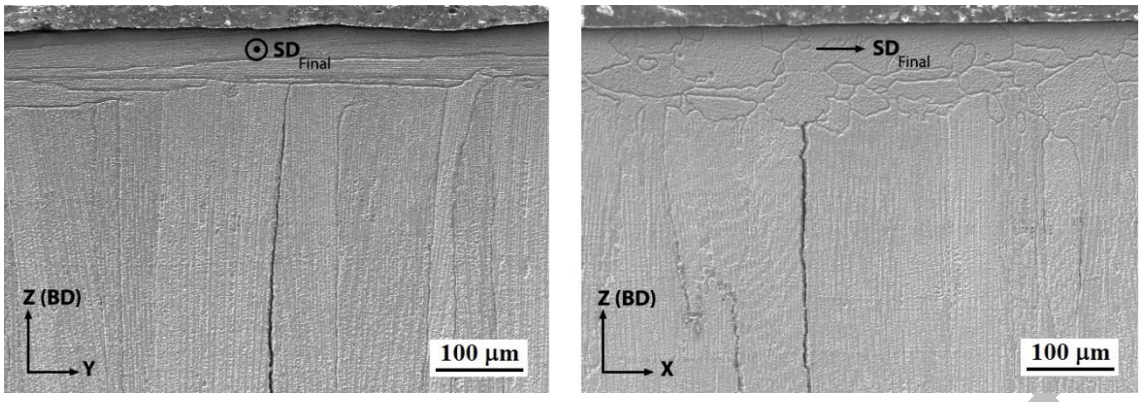

(a)

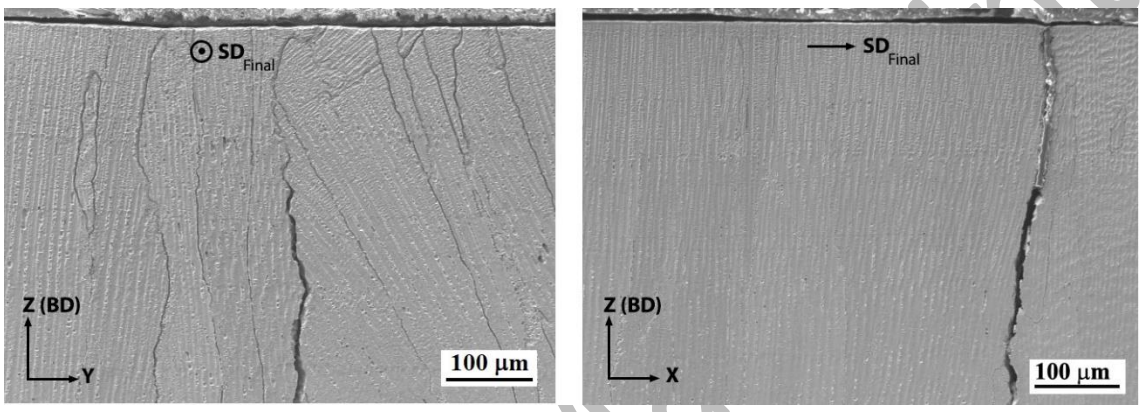

(b)

Fig. 5 Cross section micrographs of samples built with (a) F25 condition and (b) F50 condition. For both (a) and (b), left: y-z cross section and right: x-z cross section.

For condition F50, there were no horizontal dendrites to cover the cracks. Thus, cracks have grown to the surface, as can be seen in Fig. 4b. In Fig. 5b, the cracks appearing in both x-z and y-z cross sections are similar because intercolumnar grain boundaries should appear similar when samples are sectioned parallel to BD. However, in regard to the appearance of the irregular cracks in Fig. 4b, the cracks orientated, to some extent, normal to the SD on the sample surface. During EBPBF, it is common to change the SD by 90° after every layer. Thus, if there is an orientational preference of hot cracking that is due to the directional preference of stress relating to the SD, the orientation of cracking should be alternating with each layer, following the change of SD after each layer. However, cracks that were predominantly straight and crossing many layers in the BD that are shown in Fig. 5, and cracks appearing more normal to SD on surface in Fig. 4b, need to be reconciled. For this reason, an examination of cracks, in sample with F50, but viewing them on consecutive x-y cross sections (normal to BD) is presented below.

3.2 Crack networks observed through consecutive sectioning

Cracks are now examined by viewing the cracks in each consecutive layer to see how the cracks have grown. An illustration of layers in an x-z cross section of sample F50 is shown in Fig. 6. The top layer was approximately 120 μm in thickness. The thickness of all other layers should be on average 70 μm, which is the distance the base plate moved downward after each layer. Thus, in this F50 condition, ~ 50 μm in thickness of the top layer material was remelted in each layer. As

indicated in Fig. 6, half of the track width ($W_{Tk}/2$) was over 500 μm. This is consistent with the beam size specified with Arcam SEBM machine that beam size ranges 400 to 1000 μm. F50 is a low beam focus condition and thus W_{Tk} higher than 1000 μm is reasonable.

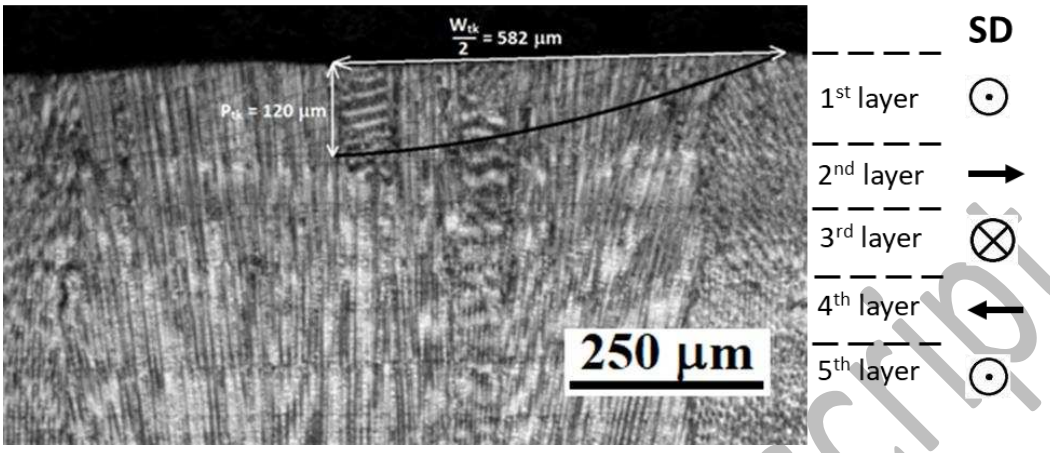

Fig. 6 Micrograph taken in an x-z cross section of sample F50 indicating the various layers including the top (1st) layer. Scan directions are indicated by arrows and by ⊙ and ⊗ as normal to image plane but opposite to each other. Note: The micrograph was taken with the image intentionally out-focused slightly to observe track boundaries.

As described in Experimental procedure (2.1), progressively polishing through the layers has been conducted, so as to view the x-y cross section of each of these 5 layers indicated in Fig. 6. These images of x-y cross sections of layers are shown in Fig. 7. In the low magnification images (Fig. 7a), the irregular (rugged) cracks were orientated more in the direction normal to the SD_{Final} (similar to those appeared in Fig. 4b) and are clearly seen in each layer. This means that cracks observed in layer 1 were the cracks grown from many layers below. Observation of these x-y cross sections have revealed another feature: irregular cracks that are more aligned with SD_{Final} were revealed when polishing deeper through the layers. To illustrate this, areas 1-4 are outlined in Fig. 7a. In each of these outlined areas, there were no cracks in the first or second layer but in subsequent layers, cracks were present along the grain boundaries and orientating more parallel to SD_{Final}.

An example of a crack going through the layers at a higher magnification is illustrated in Fig. 7b for area 1 in Fig. 7a. Gradually what is revealed is a crack that is closely aligned to SD_{Final}. In the top layer (layer 1 in Fig. 7b), dendrite filled grains can be seen but no crack was observed in this small area (area 1). In layer 2, cracks were still largely absent. In layer 3, a crack which appears to be discontinuous could be seen. The crack was clearer in layer 4, and in layer 5 the crack was continuous. It is very clear that the crack followed the columnar grain boundaries. Viewing the x-y plane, the grains were largely equiaxed and the path along the grain boundaries was irregular (rugged). Thus, although the crack in area 1 after the top two layers was more aligned with SD_{Final}, it also appears irregular in shape. This is also the reason that cracks appeared in the sample surface as quite irregular shape although they orientate more normal to SD, as in Fig. 4b.

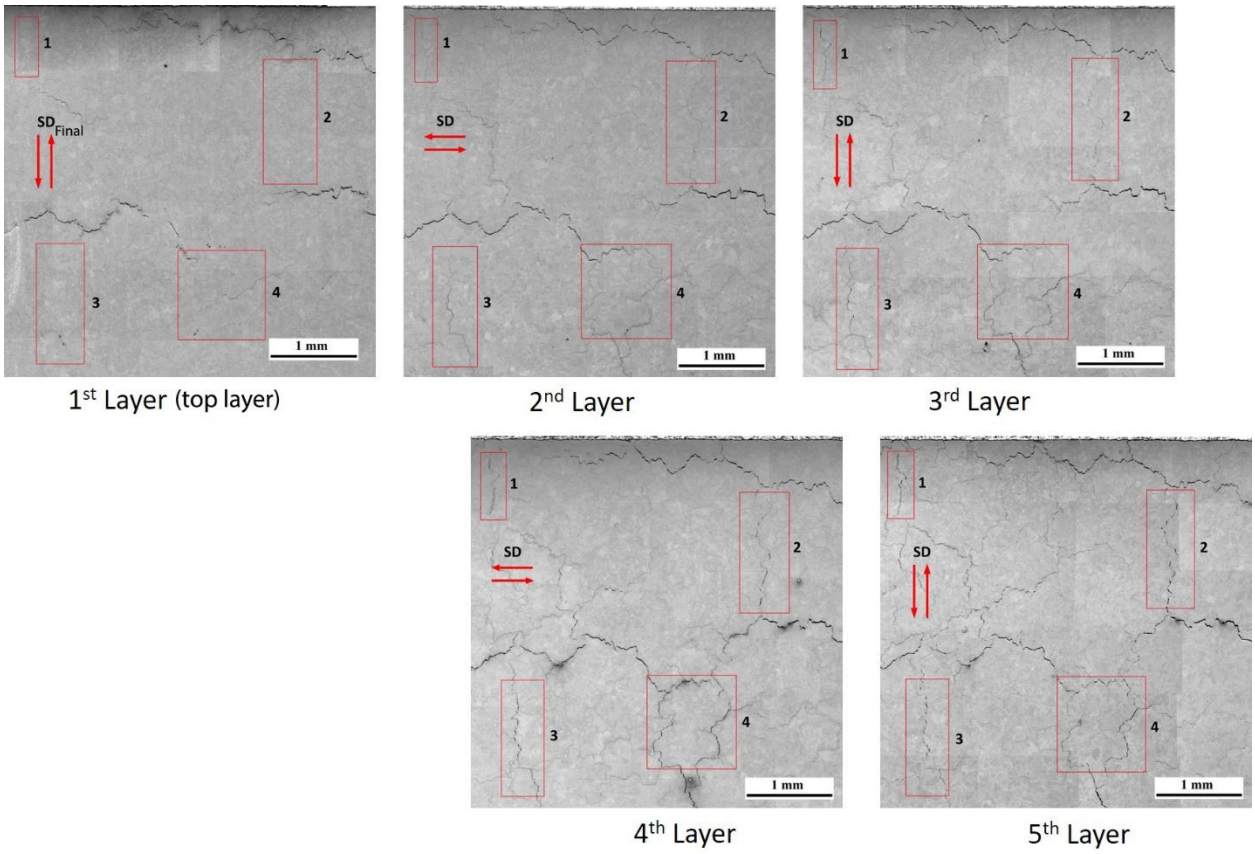

(a)

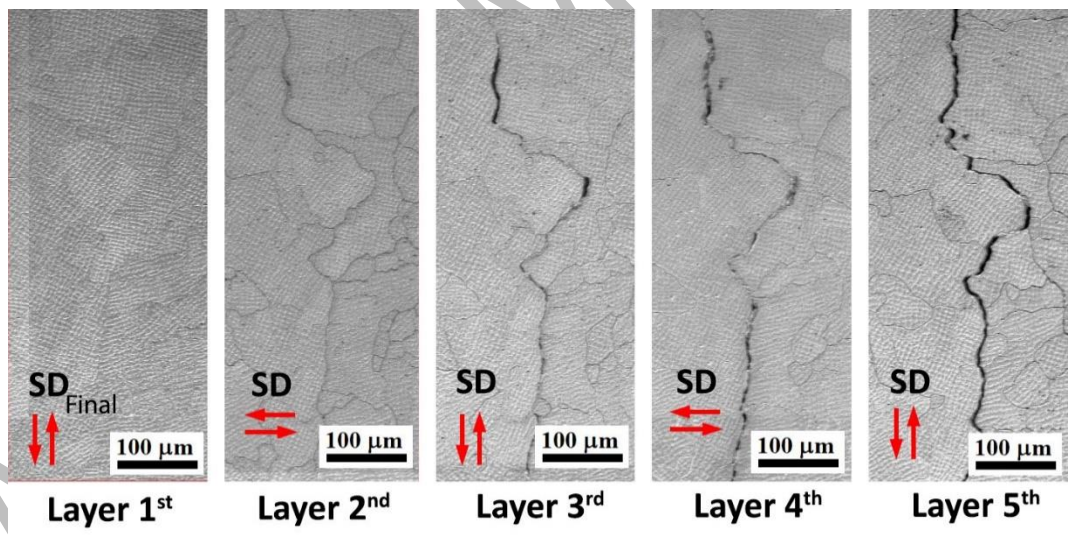

(b)

Fig. 7 Progressive cracks in F50 sample: (a) an x-y cross section micrograph of each layer as indicated, and (b) higher magnification micrograph of the small area 1 in (a) for each layer.

The sequence of the area 1 crack development (crack 1) suggests that, if there was another layer (layer 0 on top of layer 1), the area 1 crack would have actually grown to the sample surface, after hypothetical layer 0. This is because during the layer 0 building the crack would be more normal to SD_{Final}. In other words, if there was a layer 0, area 1 crack should be seen in all the layers from layer 0 to layer 5. For the same reasoning, before layer 1 (last layer), there was an area 1 crack in

layer 2. It can be reasoned that here during the melting of layer 1, liquid has back filled the area 1 crack found in layer 2, but re-cracking has not occurred, as the stress state during layer 1 building was adverse to the formation of hot tearing in layer 1, and in liquation cracking (re-cracking) in layer 2. The fact that the area 1 crack in layer 3 and layer 4 may not be fully continuous has suggested that liquid back filling may actually have reached layer 4, at least locally.

The above discussion suggests a mechanism explaining how a crack may start growing and stop growing alternatingly following the alternating SD. This is illustrated schematically in Fig. 8a. Starting with layer 4, during solidification, the hot crack along the dendrite grain boundary has grown at a starting point from the liquated boundary of columnar grains. During layer 3 scanning, liquid has backed filled the crack below the melt track for a distance, and no liquation and solidification cracking occurs, as the direction of thermal stress is not favourable for cracking. During layer 2 solidification, however, thermal stress is favourable for cracking (liquation cracking first and then hot tear). The scanning process in the top layer (layer 1) is the same as that in layer 3, and thus no cracking occurs in both layer 1 and largely layer 2. Cycles of cracking and healing locally repeat, alternatingly for the top two layers as building progresses, resulting in the actual growth of a long crack. Hot tearing occurs in each alternating cycle, but the final long cracks have actually resulted from liquation cracking.

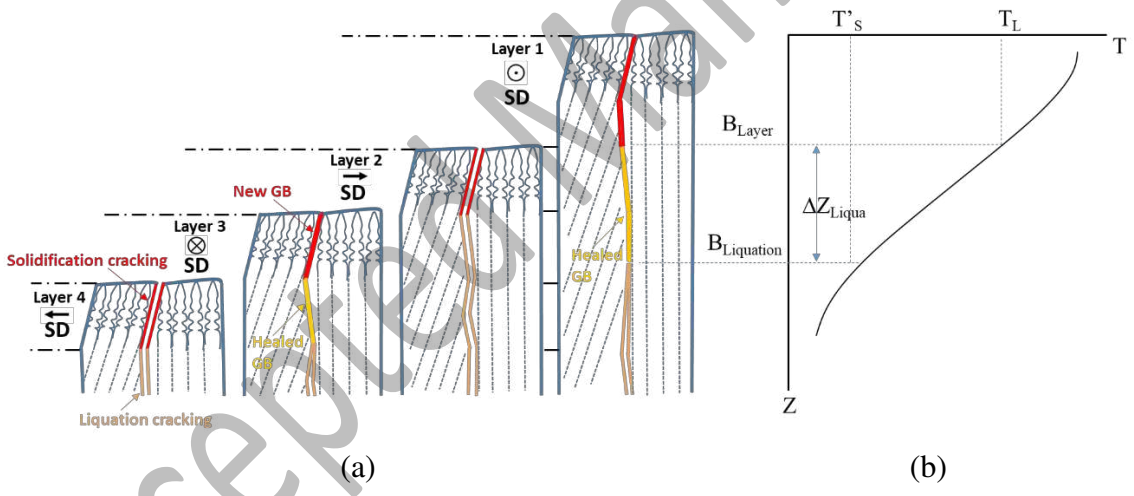

Fig. 8 Illustration of (a) hot cracking through cycles of liquation cracking and hot tearing, healing of crack and then liquation cracking and hot tearing again during building and (b) temperature distribution near track boundary.

In Fig. 6 and Fig. 7, in samples after electrolytic treatment causing etching, grain boundary cracking and grain boundaries can be clearly seen. To solely observe cracks without etching the grain boundaries, samples can be examined after mechanical polishing without having gone through the electrolytic treatment. Two images of the F50 polished sample are shown in Fig. 9. An example of a crack grown to the top surface is shown in Fig. 9a. In Fig. 9b, two cracks have terminated in that cross section, one ~ 200 µm and the other ~ 250 µm from the sample surface, and grain boundaries without having experienced hot cracking in the top region are not revealed in the polished sample. This is consistent with the crack healing and re-cracking demonstrated in Fig. 7 and the mechanism described in Fig. 8. From the crack growth mechanism identified here,

observations in the literature can be explained. For example, cracks that reach the surface shown by Chauvet et al. (2018), and crack growth to just below the last melt layer shown by Kontis et al. (2019) can thus be readily explained.

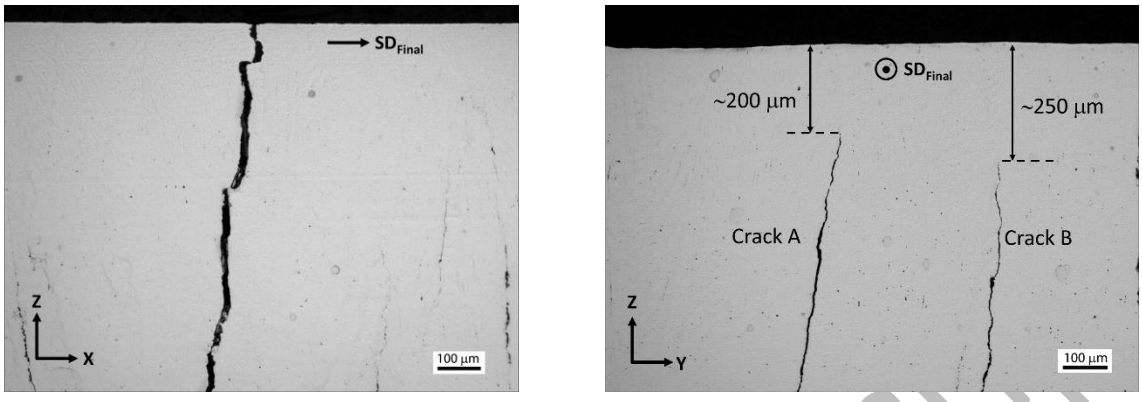

(a) (b)

Fig. 9 Cross section images of an as-polished sample built with F50 condition: (a) x-z cross section and (b) y-z cross section.

The mechanism illustrated in Fig. 8a and the depth of liquation refilling ($\Delta Z_{Liqua.}$) should correspond to the temperature distribution near the melt track boundary (B_{Layer}) as illustrated in Fig. 8b. The length of the liquid film, or $\Delta Z_{Liqua.}$ was measured from the tips of the cracks ($B_{Liquation}$) to the last layer's boundary (bottom of the melt/track) which is ≈ 120µm (for F50) from the top surface. Then, ΔZ_{Liqua} was from 80 µm (= 200 µm – 120 µm) to 130µm (= 250 µm – 120 µm), as measured from crack A and crack B in Fig. 9b. Liquid can reach the depth location (liquation boundary, $B_{Liquation}$ in Fig. 8b) at which the temperature is the last solidification point of the alloy. Thus, $\Delta Z_{Liqua.}$ is approximately equal to the solidification range ($\Delta T' = T_L - T_S'$ where T_L is the liquidus and T_S' is the actual solidus of the alloy) over the temperature gradient of solid-liquid interface ($G_{L\text{-}S'}$) at the track boundary (TB). Ronan (2010) conducted extensive measurements on the solidification range of Co-Cr-Ni-W alloy and showed that $\Delta T'$ is approximately 180 K. Then:

$$G_{L-S'} \approx \frac{\Delta T'}{\Delta Z_{Liqua.}} = \frac{180\ \mathrm{K}}{(0.8\sim1.3)\times10^{-4}\ \mathrm{m}} = (1.4\sim2.25)\times10^{6}\frac{\mathrm{K}}{\mathrm{m}} \approx 2\times10^{6}\frac{\mathrm{K}}{\mathrm{m}}$$

No detailed research has been found in literature on studying $G_{L\text{-}S}$ during EBPBF of Co-alloys. There has been, however, a series of studies on EBPBF of Ni-superalloy IN718 where $G_{L\text{-}S}$ is a major consideration. Raghavan et al. (2016) conducted numerical modelling and predict maximum $G_{L\text{-}S}$ which should be at track boundary (TB) during EBPBF of IN718 to be 5×10^6 to 1×10^7 K/m. More recently, Raghavan et al. (2017) estimated $G_{L\text{-}S}$ at TB during EBPBF to be ~ 1×10^6 K/m based on comparing the predicted value of primary dendrite arm spacing (λ_1), which was obtained based on a theoretical model of λ_1 relating to $G_{L\text{-}S}$ and $R_{L\text{-}S}$ (solidification rate), to the measured λ_1 value. The values of $G_{L\text{-}S}$ and $R_{L\text{-}S}$ were obtained based on simulation. Lee et al. (2018) also predicted, based largely on simulation, maximum $G_{L\text{-}S}$ to be between 5×10^5 and 1×10^6 K/m. The value of maximum $G_{L\text{-}S}$ at 2×10^6 K/m estimated in this work is close to the values of the more recent work of Raghavan et al. (2017) and of Lee et al. (2018).

3.3 Influence of temperature distribution on stress direction

In fusion welding, one common type of hot cracking reported is solidification cracking that normally occurs at the centreline of the weld seam. EBPBF is fundamentally a welding process. However, hot cracking observed on the top surface has been shown to be normal to SD. In other words, cracks tended to be transverse to the track's centreline. To understand how thermal stresses affecting the cracking direction, temperature distribution during EBPBF scanning of 20 tracks was investigated using the proposed numerical simulation. The melt pool shapes after a scanning of two tracks, ten tracks and 20 tracks are shown in Fig. 10a,10b and 10c respectively. In EBPBF, Karimi et al. (2018) showed that heat accumulation increases as the number of scanned tracks increases. Thus, at the 2nd track, peak temperature was recorded at 2529°C at the centre of the melt pool and increased to 2747°C at the 20th track. In addition, the melt pool shape can be observed to be significantly elongated. Considering the freezing range of the alloy reported by Ronan (2010) at around 1220-1400 °C, the melt pool after the 2nd track is around 7 mm length, as shown in Fig. 10a. Of the track 10th (Fig. 10b), due to effect of heat accumulation, the melt pool length was more than half of the track and becomes as elongated as the track length (20 mm) at the 20th track, as shown in Fig. 10c.

(a)

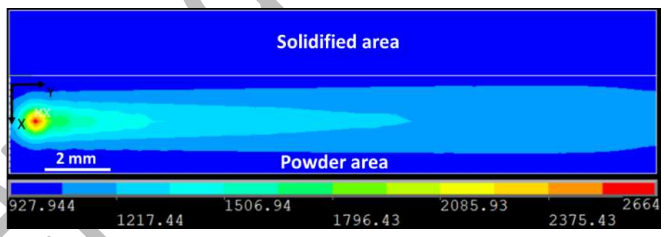

(b)

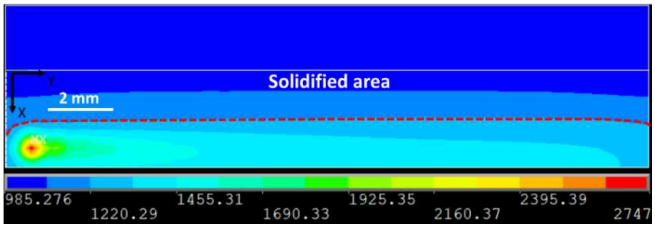

(c)

Fig. 10 Numerical simulation result of temperature distribution after: (a) the 2nd and (b) the 10th track and (c) 20th track. A red-dotted line in (c) indicates the track-length (20 mm) melt pool.

The simulation result obtained in this study has shown a good agreement with previous works that analyse a multi-tracks model for EBPBF process. Simulation models for single track, however, are

not discussed as the effect of heat accumulation is not considered. Tadano et al. (2018) obtained a half-track length melt pool for their model on a 10 mm x 10 mm x 5mm using René 80 Ni-based alloy. Plotkowski et al. (2017) employed the Rosenthal model for transient temperature analysis of EBPBF of IN718 Ni-based alloy on a scan pattern of 5mm x 5mm. The result showed that the melt pool length is track-long due to IN718 alloy's low thermal diffusivity and limited thermal conductivity caused by the high preheat temperature. Consequently, the actual advancing direction of the solidification front will not be tied to SD, but rather change to the direction of hatching (90^{o} away of SD).

The scenario depicted by Plotkowski et al. (2017) is applicable to the current study. For a layer dimension of 20 mm x 20 mm, line offset of 0.1 mm and track's width approximately at 1.1 mm (for focus offset 50 mA), there can be 188 scanning tracks within a deposited layer. This leads to the melt pool being as elongated as the track-length, as illustrated in Fig. 10c. This explains why tear-drop ripples are not seen (as has been shown in LPBF) and instead wave-front ripple dominant for both F25 and F50 samples, as observed in Fig. 4. Similar observation of wave-front melt pool was also reported by Zhao et al. (2019) in their work on EBPBF of a Co-Cr-Mo alloy. Fig. 11 illustrates how the scenario has resulted in the development of solidification cracks on the surface. At the beginning of the hatching (e.g. Track 1), solidification crack could form at the track's centreline that is similar to fusion welding. However, the small line offset (0.1 mm) together with large track's width (~1.1 mm) caused the succeeding track to overlap the previous track's centreline, and so did the solidification crack. Thus, when a new solidification crack formed, the old one disappeared as it has been remelted. Then, as the melt pool became more elongated (e.g. Track 20), the solid-liquid advancing shifted its direction from being along SD to be normal to SD, as shown in Fig. 11c. Consequently, direction of thermal stresses altered accordingly, favouring the tensile stress being more dominant and resulting in crack growth predominately normal to SD.

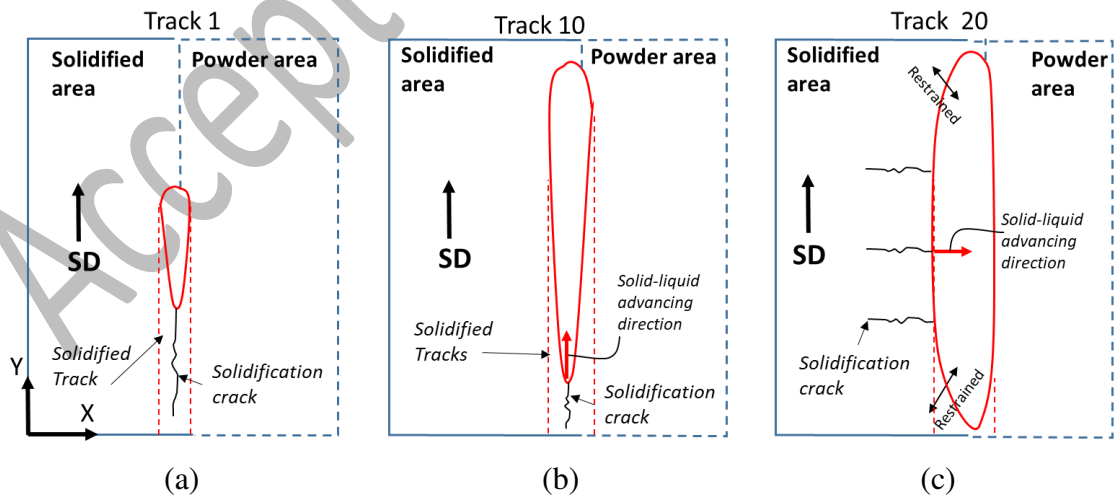

(a) (b) (c)

Fig. 11 Schematic illustration the development of the normal-to-SD solidification cracks during EBPBF, (a) melt pool and crack in Track 1; (b) melt pool and crack the 10th track and (c) Track-length melt pool results in solid-liquid advancing direction and cracks to be normal to SD.

3.4 Crack growth and grain orientations

In MAM, the misorientation angle of neighbouring grains has been viewed as an important factor affecting hot cracking. Chen et al. (2016) reported that most of the observed liquation cracks in their laser additive manufactured IN-718 alloy occurred at misorientation angles > 30°. Han et al. (2018) found that hot cracks preferentially formed at high angle grain boundaries in their LPBF of Hastelloy X. In EBPBF of a Ni-based alloy, Chauvet et al. (2018a) observed high frequency of cracks at grain boundaries > 15°. The critical grain boundary angle (of 13°) to distinguish low and high angle grain boundaries can be referred to the theoretical and experimental work of Wang et al. (2004).

In this present work, EBSD scanning was conducted in an x-y plane of a sample to better reveal the effect of misorientation angle on hot cracking. Thus, the direction normal to the sample x-y plane was the direction of sample normal in the reference frame according to the convention of reference directions in sample positioning for EBSD scanning/mapping. The rolling direction aligned with x-axis and the transverse direction aligned with y-axis. The values of misorientation of neighbouring grains corresponding to a local crack network in a sample is presented in Fig. 12. For clarity, the crack network in Fig. 12a was traced and superimposed in the EBSD orientation maps in Fig. 12b. In the "normal" map (left of Fig. 12b), the colour difference is small, meaning there was a preferred growth along BD. In the other two maps, it is clear, that the colours of both sides along a crack are highly different, meaning a high angle of misorientation.

Table 2 lists the misorientation angles of neighbouring grains. The three values in red are for GBs next to but not part of the crack path. Misorientation angles of GBs in the crack network were high ranging from 29.8° to 51.3°, except GB10 for which the angle was low at 13.7°. This means that a low angle GB can also be a small part of a crack path, which is necessary for the main crack network to be connected. In other words, a small distance of low misorientation angle grain boundary can also crack leading to bridging of the main cracks. GB3 was next to the crack path and as it was low angle misorientation, cracking did not select this GB to form a crack path. GB4 was a high angle boundary but, as GB3 was a low angle GB and thus had not cracked, there was not a crack that propagated through to GB4. Instead, cracking occurred on the other side of the grain where it bordered the next grain in a high misorientation angle. For the same reason, the relatively low angle of GB8 has not become part of the crack path. These features of grain misorientations affecting the development of crack network can be revealed better in EBSD maps of an x-y plane, as in Fig. 12, than those in maps presented in the literature normally based on EBSD scanning in x-z or y-z planes.

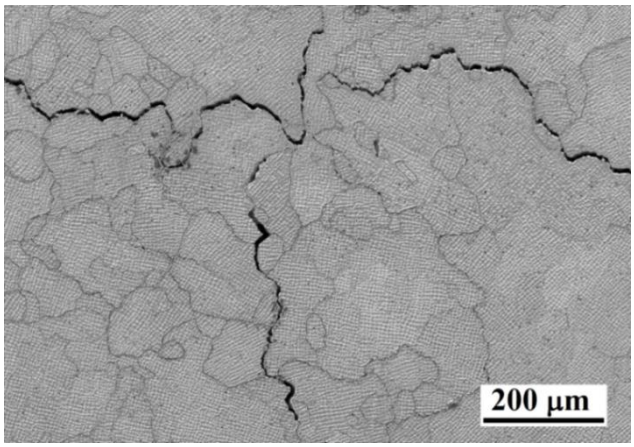

(a)

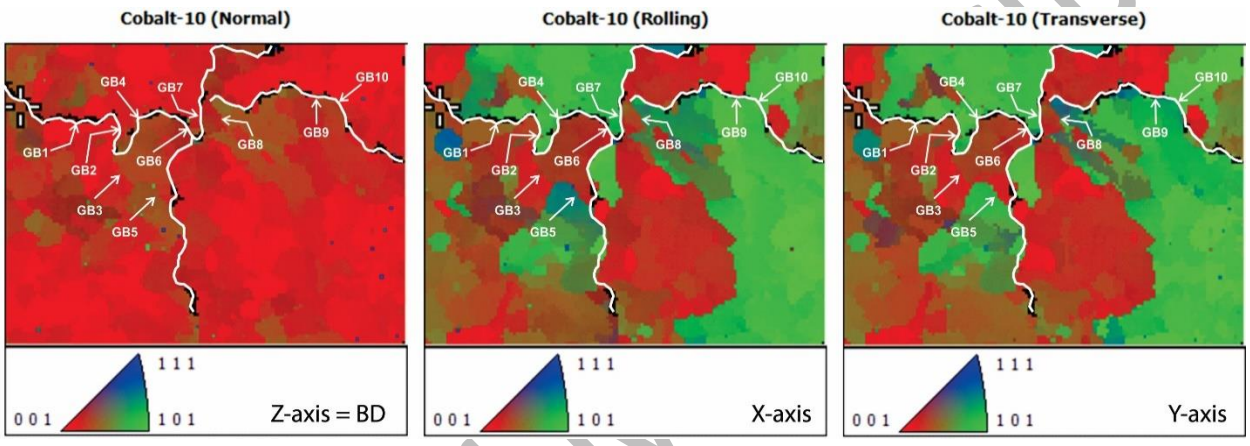

(b)

Fig. 12 Crack network shown in x-y plane by (a) SEM micrograph and (b) EBSD maps with the network indicated by the while and irregular lines and GB1 to GB10 indicated where grain misorientations have been determined (and listed in Table 2).

Table 2 Grain boundary (GB) number and the corresponding misorientation angle of the two neighbouring grains.

GB no	GB1	GB2	GB3	GB4	GB5	GB6	GB7	GB8	GB9	GB10
Angle	30.4°	28.8°	14.5°	39.0°	37.3°	51.3°	46.0°	22.9°	45.4°	13.7°

3.5 Demonstration of crack-free H-V grain growth

Microstructures of the samples fabricated using the two EBPBF conditions, $E_{Vol\text{-}2}$ and $E_{Vol\text{-}3}$, are shown in Fig. 13. Clearly in these two micrographs, the H-dendrite layer has been retained in each layer and has disrupted the long columnar grain growth in the build direction. The retaining of the H-dendrite layer in each layer scan provided no condition for cracks to grow along or close to BD. There was also no liquation cracking in H-dendrite layers as in these layers, dendrite grain boundaries were also aligned largely horizontally. Thus, cracks have not been observed in these samples. In the $E_{Vol\text{-}2}$ sample, as predicted, lack of fusion (LOF) has been detected (Fig. 13a), but the $E_{Vol\text{-}3}$ sample was largely free of LOF (Fig. 13b). Fig. 13b also shows that, in the top layer, vertical columnar grains have grown from the H-dendrite layer but these grains could not grow to

the surface in the same direction. Instead, from middle of the layer, H-dendrites have grown with thickness of ~140 μm. This indicates that, as maybe indicative in Fig. 13b, the E_{Vol-3} condition has resulted in a deep (~ 325 μm) and a track of a low tangent angle.

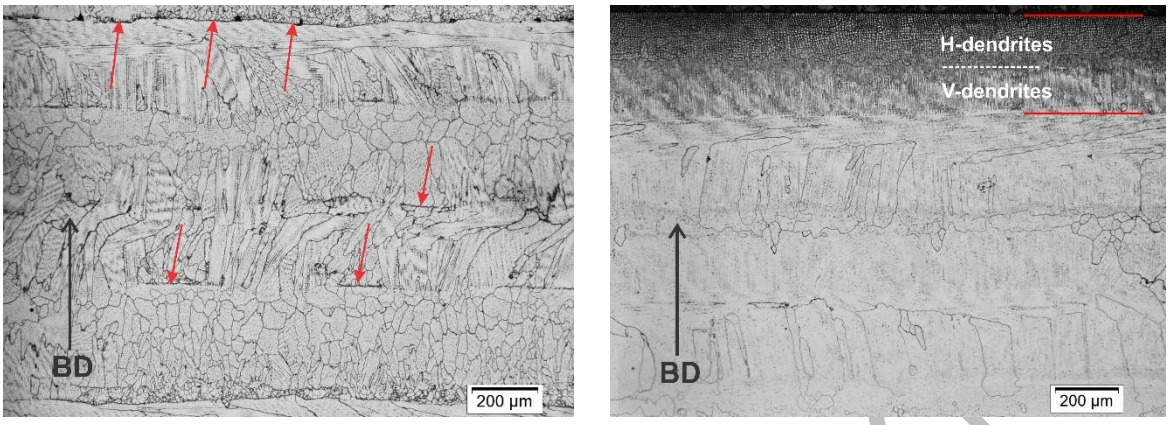

(a) (b)

Fig. 13 Optical x-y plane micrographs of (a) E_{Vol-2} and (b) E_{Vol-3} samples displaying each build layer comprising a horizontal and a vertical columnar grain layer. In (a) red arrows point to lack of fusion. In (b) the two red lines indicate the top/final layer within which H- and V-dendrite portions are marked.

The grain structure in a location of an E_{vol-3} sample has been examined further and the SEM micrographs are shown in Fig. 14. The low magnification micrograph shown in Fig. 14a illustrates again that in each scan layer there were two sublayers. As the scan direction changes by 90^o every layer, H-dendrites can be seen changing their growth direction accordingly. The growth of V-dendrites on a H-dendrite layer is further revealed in a higher magnification SEM micrograph in Fig. 14b, which clearly shows that the V-dendrites have epitaxially grown from the H-dendrite. The growth of each V-dendrite (trunk) should be normal to the primary trunk and has likely grown from a secondary arm of the H-dendrite.

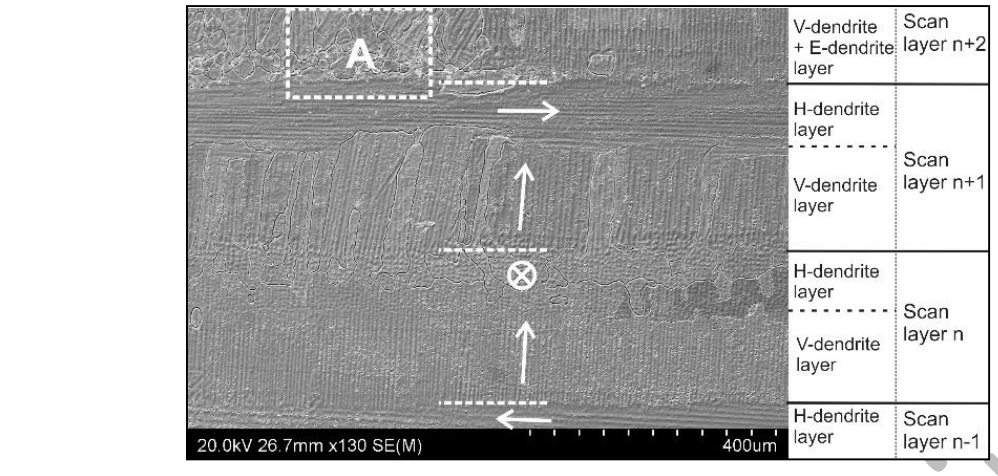

(a)

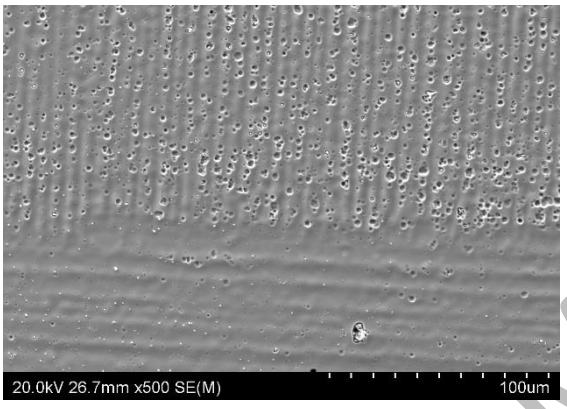

(b)

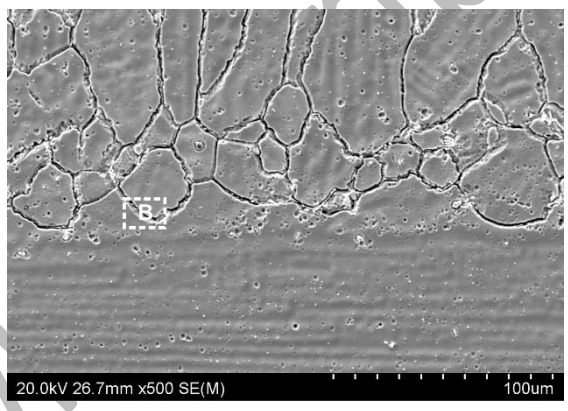

(c)

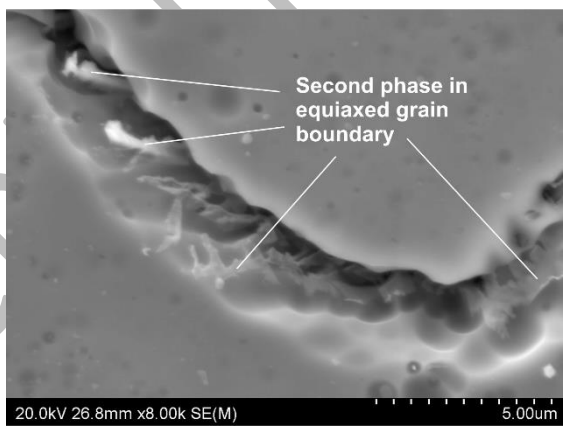

(d)

Fig. 14 SEM micrographs taken in x-y plane of a $E_{Vol\text{-}3}$ sample: (a) showing two sub layers within a scan layer with grain growth directions indicated by arrows or by ⊗ as normal to the image plane, (b) showing V-dendrites having grown from H-dendrites, (c) showing equiaxed grains in area marked "A" in (a) having grown from H-dendrites, (d) showing second phase under a high magnification in location marked "B" in (c).

The micrograph in Fig. 14a includes from the bottom a partial scan layer (layer n-1), two full scan layers (layers n and n+1) to follow and then another partial scan layer (layer n+2) in the top. The partial (n-1)th layer was part of the H-dendrite layer having grown towards left and having partially

melted during the nth layer scan. During the nth layer scan, V-dendrites have grown from the un-melted H-dendrite beneath in the (n-1)th layer epitaxially. The V-dendrite grains have grown for 140 to 180 μm, before being out-grown by the H-dendrite layer (which has grown in a direction normal to the micrograph plane). As it is shown in Fig. 13b, the top layer was ~325 μm in thickness. The scan layer thickness was set for 300 μm. Thus, the portion of the H-dendrite layer in the nth layer that was melted during the (n+1)th layer scan should be ~25 μm in thickness. V-dendrites have grown epitaxially from the nth layer H-dendrites for ~180 μm before being out-grown by a H-dendrite layer again, during the (n+1)th layer scan, as is clearly shown in Fig. 14a. This (n+1)th H-dendrite layer, which could be ~140 μm in thickness, then melted off for ~25 μm in the (n+2)th layer scan before another epitaxial growth.

During grain growth in the (n+2)th layer, a new growth mode had occurred in part of the layer. As it is shown in Fig. 14a, in the top and (n+2)th layer, the left half is morphologically different from the epitaxial and then columnar dendritic growth on the right half. A higher magnification micrograph taken in a small area marked "A" in Fig. 14a and shown in Fig. 14c shows two features. First, similar to what is shown in Fig. 14b, the H-dendrite in Fig. 14c has been partially melted as there is no evidence of lack of fusion. Second, there was little epitaxial growth from the un-melted H-dendrite below and instead equiaxed grains have nucleated and grown. The equiaxed grain layer was 2-3 grains in thickness. The presence of these equiaxed grains has suggested the present $E_{Vol\text{-}3}$ solidification condition being in general close to and locally being the condition of the alloy that a layer of equiaxed grains could form next to the bottom track boundary.

The local presence of the equiaxed grain layer may be compared to the bimodal structure with a layer of equiaxed grains adjacent to the track boundary followed by columnar grains into the track during LPBF of Scalmalloy (Al-4Mg alloy containing Sc and Zr). The Al_3(Sc,Zr) particles formed during solidification in the previous track can survive in a short distance from track boundary during the melting in the next track/layer scan as reported by Spierings et al. (2018). The survived Al_3(Sc,Zr) particles then act as grain nuclei for the subsequent equiaxed grain growth. Solidification of the present Co-based alloy also results in second phase (eutectic) solidification in intergranular areas, as shown in Fig. 14d. It may be suggested that melting of the second phase particles may not be complete in the low temperature region and, next to track boundary, the un-melted particles may act as grain nuclei for equiaxed grain solidification.

The equiaxed grains are clearly shown in the top-left area of the EBSD orientation map in Fig. 15. For this EBSD scanning, direction normal to the sample x-z plane was the normal direction in the reference frame. The mapped area is only slightly less than the area of the image in Fig. 14a. With the exception of the equiaxed grain area, the rest has appeared {001} or close to {001} in all maps (rolling, normal and transverse). This may be at least partially explainable if the effect of H-dendrite layer on crystal growth is considered. In Fig. 14a, the (n-1)th H-dendrite layer has grown to the left meaning one of the {001}, thus appearing red in Fig. 15. The V-dendrites in the nth layer, having grown from the (n-1)th H-dendrite layer and parallel to the image plane that was another {001} plane. The plane of the H-dendrite layer in the nth was also a {001}. This is because of the branching out of V-dendrites when they have grown to the upper half of the track. This was

the same for (n+1)th H-dendrite layer. The location disruption of the growth continuing with {001} was when locally equiaxed grain solidification has occurred.

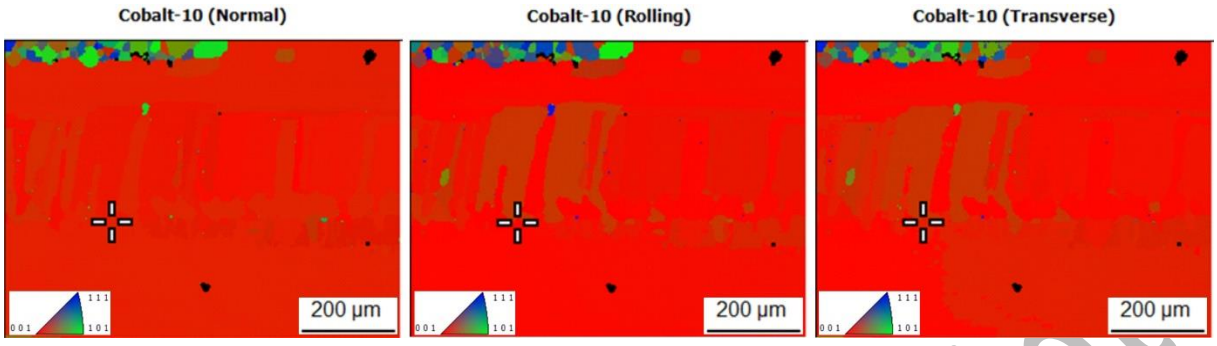

Fig. 15 EBSD orientation map of the area within and slightly smaller than the area shown in image area of Fig.14a.

Conclusions

How cracks developed during electron beam powder bed fusion (EBPBF) of a difficult-to-weld Co-Cr-Ni-W alloy and a possible remedy have been revealed and demonstrated, respectively, in this study:

1. Crack networks readily developed using commonly used EBPBF parameters but whether cracks were observed in the sample surface depended on the dendrite orientation in the final solidification stage. A low focus offset value and thus a more focused beam resulted in the growth of horizontal dendrites in the top region of the top layer, stopping crack growth to the surface. Through consecutive sectioning, hot tearing has been shown to combine with liquation cracking for crack networks to grow vertically. Alternatingly, crack healing was observed during a layer but then crack growth occurred in the subsequent layer of building. The length of the liquation healing has suggested the maximum thermal gradient to have reached 2×10^6 K/m.
2. Numerical simulation showed the significant effect of heat accumulation in multi-tracks scanning on the elongation of the melt pool. Consequently, the advancing of solid-liquid interface has shifted from the scanning to the hatching direction. This has led to the development of predominant tensile stress along the scanning direction, which explains the observation of crack orientation on the samples' surface.
3. Using EBSD, it was found that a crack path was likely to be normally along the grain boundaries with high misorientation angle. However, a low misorientation angle grain boundary was also shown to be a small part of such crack paths. It is also apparent that a high misorientation angle grain boundary did not tend to crack if nearby cracking has occurred and has already released the thermal stress during solidification.
4. Grain growth control utilising horizontally grown dendrites (H-dendrite) can stop columnar grains to grow beyond one layer. This has been demonstrated by using a special layer thickness and spacing combination so that the H-dendrite layer has grown to over 140 µm and was only

partially melted off in the layer immediately after. Thus, solidification in each layer has mostly started epitaxially with columnar-dendrites grown vertically before being out-grown by another layer of H-dendrites. The condition used was close to equiaxed grain solidification condition and locally, instead of epitaxial growth, equiaxed grain solidification has occurred.

References

Babu, S. S., N. Raghavan, J. Raplee, S. J. Foster, C. Frederick, M. Haines, R. Dinwiddie, M. K. Kirka, A. Plotkowski, Y. Lee and R. R. Dehoff (2018). "Additive Manufacturing of Nickel Superalloys: Opportunities for Innovation and Challenges Related to Qualification." Metallurgical and Materials Transactions A **49**(9): 3764-3780.

Chandra, S., Tan, X., Narayan, R.L., Wang, C., Tor, S.B. and Seet, G (2021). "A generalised hot cracking criterion for nickel-based superalloys additively manufactured by electron beam melting." Additive Manufacturing **37**:101633.

Chauvet, E., P. Kontis, E. A. Jägle, B. Gault, D. Raabe, C. Tassin, J.-J. Blandin, R. Dendievel, B. Vayre, S. Abed and G. Martin (2018). "Hot cracking mechanism affecting a non-weldable Ni-based superalloy produced by selective electron Beam Melting." Acta Materialia **142**: 82-94.

Chauvet, E., C. Tassin, J.-J. Blandin, R. Dendievel and G. Martin (2018). "Producing Ni-base superalloys single crystal by selective electron beam melting." Scripta Materialia **152**: 15-19.

Chen, Y., F. Lu, K. Zhang, P. Nie, S. R. E. Hosseini, K. Feng and Z. Li (2016). "Dendritic microstructure and hot cracking of laser additive manufactured Inconel 718 under improved base cooling." Journal of Alloys and Compounds **670**: 312-321.

Cloots, M., P. J. Uggowitzer and K. Wegener (2016). "Investigations on the microstructure and crack formation of IN738LC samples processed by selective laser melting using Gaussian and doughnut profiles." Materials & Design **89**: 770-784.

DebRoy, T., T. Mukherjee, J. O. Milewski, J. W. Elmer, B. Ribic, J. J. Blecher and W. Zhang (2019). "Scientific, technological and economic issues in metal printing and their solutions." Nature Materials.

Eskin, D. and Katgerman, L. (2004). Mechanical properties in the semi-solid state and hot tearing of aluminium alloys. Progress in Materials Science 49: 629-711

Han, Q., R. Mertens, M. L. Montero-Sistiaga, S. Yang, R. Setchi, K. Vanmeensel, B. Van Hooreweder, S. L. Evans and H. Fan (2018). "Laser powder bed fusion of Hastelloy X: Effects of hot isostatic pressing and the hot cracking mechanism." Materials Science and Engineering: A **732**: 228-239.

Karimi, P., E. Sadeghi, P. Åkerfeldt, J. Ålgårdh and J. Andersson (2018). "Influence of successive thermal cycling on microstructure evolution of EBM-manufactured alloy 718 in track-by-track and layer-by-layer design." Materials & Design **160**: 427-441.

Kontis, P., E. Chauvet, Z. Peng, J. He, A. K. da Silva, D. Raabe, C. Tassin, J.-J. Blandin, S. Abed, R. Dendievel, B. Gault and G. Martin (2019). "Atomic-scale grain boundary engineering to overcome hot-cracking in additively-manufactured superalloys." Acta Materialia **177**: 209-221.

Lee, Y., M. M. Kirka, J. Ferguson and V. C. Paquit (2020). "Correlations of cracking with scan strategy and build geometry in electron beam powder bed additive manufacturing." Additive Manufacturing **32**: 101031.

Lee, Y. S., M. M. Kirka, R. B. Dinwiddie, N. Raghavan, J. Turner, R. R. Dehoff and S. S. Babu (2018). "Role of scan strategies on thermal gradient and solidification rate in electron beam powder bed fusion." Additive Manufacturing **22**: 516-527.

Peng, H., Y. Shi, S. Gong, H. Guo and B. Chen (2018). "Microstructure, mechanical properties and cracking behaviour in a γ′-precipitation strengthened nickel-base superalloy fabricated by electron beam melting." Materials & Design **159**: 155-169.

Phan, M., D. Fraser, S. Gulizia and Z. Chen (2018). "Horizontal growth direction of dendritic solidification during selective electron beam melting of a Co-based alloy." Materials Letters **228**: 242-245.

Plotkowski, A., M. M. Kirka and S. Babu (2017). "Verification and validation of a rapid heat transfer calculation methodology for transient melt pool solidification conditions in powder bed metal additive manufacturing." Additive Manufacturing **18**: 256-268.

Raghavan, N., R. Dehoff, S. Pannala, S. Simunovic, M. Kirka, J. Turner, N. Carlson and S. S. Babu (2016). "Numerical modeling of heat-transfer and the influence of process parameters on tailoring the grain morphology of IN718 in electron beam additive manufacturing." Acta Materialia **112**: 303-314.

Raghavan, N., S. Simunovic, R. Dehoff, A. Plotkowski, J. Turner, M. Kirka and S. Babu (2017). "Localized melt-scan strategy for site specific control of grain size and primary dendrite arm spacing in electron beam additive manufacturing." Acta Materialia **140**: 375-387.

Ramirez, D. A., L. E. Murr, E. Martinez, D. H. Hernandez, J. L. Martinez, B. I. Machado, F. Medina, P. Frigola and R. B. Wicker (2011). "Novel precipitate–microstructural architecture developed in the fabrication of solid copper components by additive manufacturing using electron beam melting." Acta Materialia **59**(10): 4088-4099.

Ronan, K. P. (2010). The Effects of Small Changes in Alloy Chemistry on the Solidification Behaviour of the Cobalt-Base Superalloy FSX-414 Master Thesis, Auburn University.

Spierings, A. B., K. Dawson, P. J. Uggowitzer and K. Wegener (2018). "Influence of SLM scan-speed on microstructure, precipitation of Al3Sc particles and mechanical properties in Sc-and Zr-modified Al-Mg alloys." Materials & Design **140**: 134-143.

Tadano, S., T. Hino and Y. Nakatani (2018). "A modeling study of stress and strain formation induced during melting process in powder-bed electron beam melting for Ni superalloy." Journal of materials processing technology **257**: 163-169.

Wang, N., S. Mokadem, M. Rappaz and W. Kurz (2004). "Solidification cracking of superalloy single-and bi-crystals." Acta Materialia **52**(11): 3173-3182.

Zhao, Y., Y. Koizumi, K. Aoyagi, K. Yamanaka and A. Chiba (2019). "Manipulating local heat accumulation towards controlled quality and microstructure of a Co-Cr-Mo alloy in powder bed fusion with electron beam." Materials Letters **254**: 269-272.